J. Fluid Mech. (2020), *vol.* 892, A12. © The Author(s), 2020.
Published by Cambridge University Press
doi:10.1017/jfm.2020.177

A novel subcritical transition to turbulence in Taylor–Couette flow with counter-rotating cylinders

Christopher J. Crowley[1,†], Michael C. Krygier[1], Daniel Borrero-Echeverry[2], Roman O. Grigoriev[1] and Michael F. Schatz[1]

[1]Center for Nonlinear Science and School of Physics, Georgia Institute of Technology, Atlanta, GA 30332, USA

[2]Department of Physics, Willamette University, Salem, OR 97301, USA

(Received 30 August 2019; revised 13 December 2019; accepted 27 February 2020)

The transition to turbulence in Taylor–Couette flow often occurs via a sequence of supercritical bifurcations to progressively more complex, yet stable, flows. We describe a subcritical laminar–turbulent transition in the counter-rotating regime mediated by a transient intermediate state in a system with an axial aspect ratio of $\Gamma = 5.26$ and a radius ratio of $\eta = 0.905$. In this regime, flow visualization experiments and numerical simulations indicate the intermediate state corresponds to an aperiodic flow featuring interpenetrating spirals. Furthermore, the reverse transition out of turbulence leads first to the same intermediate state, which is now stable, before returning to an azimuthally symmetric laminar flow. Time-resolved tomographic particle image velocimetry is used to characterize the experimental flows; these measurements compare favourably to direct numerical simulations with axial boundary conditions matching those of the experiments.

Key words: transition to turbulence, bifurcation, Taylor–Couette flow

1. Introduction

The transition to turbulence in many flows falls into two classes: subcritical transitions, whereby the transition is directly from laminar flow to turbulence, or supercritical transitions, where the transition occurs through a sequence of intermediate stable flow states before ultimately ending in turbulence. By describing well the growth of infinitesimal disturbances, linear stability theory has often enabled good predictions of the critical Reynolds numbers at which supercritical transitions occur. By contrast, subcritical transitions result from the nonlinear growth of finite amplitude perturbations; therefore, linear stability analyses provide little insight into this type of transition. Subcritical transitions exhibit hysteresis, in which the turbulent flow returns back to the laminar state at a Reynolds number that is lower than that for the transition from laminar flow to turbulence.

† Email address for correspondence: chris.crowley@gatech.edu

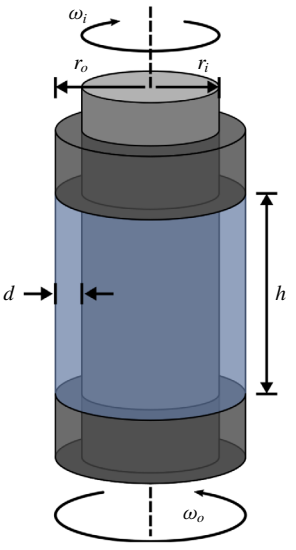

FIGURE 1. In Taylor–Couette flow, a fluid is confined between coaxial cylinders of radii r_i and r_o, which counter-rotate with angular velocities ω_i and ω_o, respectively. In the axial direction, the flow is bounded by two end caps that rotate with the outer cylinder and are separated by a distance h. In the radial direction, the separation between the cylinders is $d = r_o - r_i$. The flow is periodic in the azimuthal direction.

Both super- and subcritical turbulent transitions can be observed in the flow between two independently rotating, coaxial cylinders, or Taylor–Couette flow (TCF) (see figure 1). TCF can be uniquely characterized by four non-dimensional parameters. Two parameters characterize the geometry of the system: the radius ratio $\eta = r_i/r_o$, where r_i and r_o are the radii of the inner and outer cylinders, respectively, and the aspect ratio $\Gamma = h/d$, where $d = r_o - r_i$ is the radial separation distance between the cylinders and h is the axial height of the flow domain. The other two parameters, the inner and outer Reynolds numbers $Re_{i,o}$, describe the cylinders' rotation rates and are given by

$$Re_{i,o} = \frac{r_{i,o}\omega_{i,o}\, d}{\nu}, \tag{1.1}$$

where ν is the kinematic viscosity of the fluid and $\omega_{i,o}$ are the angular velocities of the inner and outer cylinders, respectively. By convention Re_i is always taken to be positive, whereas Re_o is positive when the cylinders are co-rotating and negative when they are counter-rotating.

Numerous studies of supercritical transitions to turbulence in TCF have been published (see, e.g. Coles (1965), Andereck, Liu & Swinney (1986), Tagg (1994) and Meseguer *et al.* (2009*b*)). Experimental studies mostly focus on geometries with $\Gamma \gg 1$ to reduce the influence of the axial boundaries on the flow and investigate transition at fixed Re_o while quasi-statically increasing Re_i. In this parameter regime, TCF exhibits a multitude of stable non-turbulent flow states for different rotation rates (Coles 1965; Andereck *et al.* 1986). As Re_i is increased, each new transition typically yields a flow of increased complexity until the flow eventually becomes turbulent.

The subcritical transition to turbulence in TCF has a long history (Couette 1890; Mallock 1896; Wendt 1933; Taylor 1936*a*,*b*; Schultz-Grunow 1959; Coles 1965; Van Atta 1966; Andereck *et al.* 1986; Prigent & Dauchot 2005). Recently, there has been renewed interest in this regime as a testbed for ideas explaining the subcritical transition to turbulence from the viewpoint of dynamical systems theory (Meseguer *et al.* 2009*a*; Borrero-Echeverry, Schatz & Tagg 2010; Avila & Hof 2013; Maretzke, Hof & Avila 2014; Lopez 2016) and as a model for understanding the source of the enhanced angular momentum transport observed in astrophysical disks, which is purportedly caused by turbulence despite the predicted stability of these flows (Richard & Zahn 1999; Ji *et al.* 2006; Paoletti & Lathrop 2011; Burin & Czarnocki 2012; Edlund & Ji 2014). In these studies, which were mostly conducted with $\Gamma \gg 1$, transition is typically observed to take place directly from the laminar base flow.

The subcritical transition to turbulence is commonly associated with wall-bounded shear-driven flows in channels, pipes and boundary layers in which two general transition scenarios have been identified: (i) an 'amplification' scenario involving transient non-turbulent modes (Reshotko 1976) and (ii) a 'bypass' transition (Morkovin 1985). In the amplification scenario, the transition begins with the appearance of a weak structured flow (e.g. Tollmien–Schlichting waves in channel flow), which undergoes amplification by linear mechanisms until it is sufficiently large that nonlinearity takes over, and the flow breaks up into turbulence. In this scenario, the unstable structured flow acts as a transient intermediary that triggers turbulence. Operationally, the amplification transition is observed by imposing carefully controlled disturbances in flows where the ambient free-stream turbulent intensities are sufficiently low (Nishioka, Iida & Ichikawa 1975). In contrast, in the bypass transition scenario, the free-stream turbulent intensity is sufficiently large that non-turbulent structured flows are not observed (are 'bypassed') and, for sufficiently large Re, the transition occurs from featureless laminar flow directly to disordered turbulent flow. Earlier studies of the subcritical transition to turbulence in TCF, which were mostly conducted at large aspect ratios, showed that this transition typically occurs directly from the laminar base flow, i.e. via the bypass mechanism.

Here, we report a subcritical transition to turbulence in counter-rotating TCF that has some features in common with the amplification scenario found in prior work on other wall-bounded shear flows. In our TCF studies, a non-turbulent intermediary flow plays a central role in the transition. This aperiodic flow features interpenetrating spirals (IPS) with opposite helicity much akin to those that have been discovered by Andereck *et al.* (1986) at large Γ and further investigated by Coughlin & Marcus (1996). At a moderate value of $\Gamma = 5.26$, we find that IPS appear transiently in the transition from laminar to turbulent flow as Re_i is increased at fixed Re_o. If Re_i is then decreased, the turbulent flow transitions to stable IPS, which persist over a range of Re_i. As Re_i is decreased further, stable IPS eventually transition back to laminar flow.

It is important to note that both super- and subcritical transitions have been examined in earlier studies of TCF with small-to-moderate aspect ratios ($\Gamma \lesssim 5$). A rich variety of phenomena have been observed, including a plethora of asymmetric states from symmetric end cap forcing (Tavener, Mullin & Cliffe 1991), a sequence of period doubling bifurcations (Pfister *et al.* 1988) and quasi-periodic dynamics with three frequencies (Lopez & Marques 2003). These examples and many others from prior work describe transitions to non-turbulent flows, distinct from the transition to turbulence reported here.

In § 2, we outline briefly the experimental and numerical methods used in this study. Then, in § 3, we discuss the transitions between flow states with a particular emphasis on the role of the IPS. In § 4, we discuss the implications of this discovery for understanding of the subcritical transition to turbulence in TCF and, more generally, in wall-bounded shear flows; we conclude in § 5.

2. Methods

Our TCF apparatus with $\eta = 0.905$ was composed of a glass outer cylinder with a radius of $r_o = 80.03 \pm 0.02$ mm and a brass inner cylinder of radius $r_i = 72.39 \pm 0.01$ mm with a black powder coat to enhance optical contrast in flow visualization studies. The aspect ratio, $\Gamma = 5.26$, was set by two end caps, separated axially by $h = 40.2 \pm 0.05$ mm and attached to rotate with the outer cylinder. The cylinders were driven by stepper motors; to reduce vibration and to ensure uniform cylinder rotation, timing belts connected the cylinders to the motors, which were mounted separately from the TCF apparatus. Additionally, a transmission with a gear ratio of 28 : 1 was used with the inner cylinder stepper motor to increase the resolution in Re_i. While the cylinders were rotating, the rate of temperature variations in the flow was kept below 0.5 °C throughout the duration of the experiments by surrounding the outer cylinder with a liquid bath. With these measures, the total systematic uncertainty for Re_i and Re_o was below 1 %.

The flow was characterized using rheoscopic flow visualization. In some studies, the working fluid was water mixed with Kalliroscope (Matisse & Gorman 1984) at a concentration of 0.3 % by volume and had a kinematic viscosity of $\nu = 1.01$ mm^2 s^{-1} at 20 °C. Other studies were carried out using a mixture of water and a stearic-acid-based rheoscopic fluid (Borrero-Echeverry, Crowley & Riddick 2018) at a concentration of 5 % by volume with kinematic viscosity $\nu = 1.03$ mm^2 s^{-1} at 20 °C. The flows were illuminated using fluorescent lights and imaged using a single Microsoft LifeCam HD webcam oriented perpendicular to the flow domain and connected via a USB interface to a computer. The resulting digital images were analysed using a custom Matlab script to identify qualitative changes in the flow as a function of Reynolds number and indicate transitions in the flow. For each image, the script counted the total number of pixels with an intensity above a fixed threshold; different flow states exhibited different, easily distinguishable pixel counts.

Tomographic particle image velocimetry (tomo PIV) (Elsinga *et al.* 2006) was also used to perform flow measurements. In tomo PIV, particles suspended in the flow are imaged simultaneously by multiple cameras at different viewing angles, and the images are used to reconstruct the light intensity distribution in a three-dimensional (3-D) flow volume; 3-D cross-correlation of distributions reconstructed at different times enables determination of 3-D velocity fields throughout a flow volume with an approximate size of d radially, $0.75h$ axially and $2\pi r_o/10$ azimuthally. The velocity fields were determined using correlation volumes with 75 % overlap that resulted in a grid of velocity vectors with a spacing of 250 μm between neighbouring vectors and a noise level of approximately 2.5 % of the outer cylinder wall speed. Custom-made, density-matched polyester particles (25 μm–32 μm in diameter) were doped with Rhodamine 6G and suspended in the flow. The particles were illuminated with a Quantronix 527/DP-H Q-switched Nd:YLF laser. Fluorescent light emitted from the particles was collected by four Vision Research Phantom V210 high speed cameras synchronized with the laser illumination. Each camera was fitted with a 105 mm Nikon Nikkor fixed focal length lens attached via a Scheimpflug

adapter (LaVision Inc.). A low pass optical filter (Semrock BLP01-532R-25) on each camera lens attenuated, by a factor of 10^7, the scattered 527 nm wavelength laser illumination and passed, with 80 % efficiency, fluorescent light at wavelengths >532 nm. The images were then analysed using LaVision Inc.'s DaVis tomographic PIV software package. To reduce optical distortion from the outer cylinder's curved surfaces, the index of refraction of both the working fluid and the bath liquid were matched to the index of refraction of the glass outer cylinder. Index matching of the working fluid was achieved by using an ammonium thiocyanate solution prepared with a specific gravity of 1.13 and a kinematic viscosity of $\nu = 1.37$ mm^2 s^{-1} at 23 °C (Borrero-Echeverry & Morrison 2016). A small amount of ascorbic acid was added to the ammonium thiocyanate solution to mitigate reaction with trace metals (Sommeria, Meyers & Swinney 1991). Index matching of the bath liquid was achieved by a binary mixture of two mineral oils with a 68.8 % heavy viscosity oil (McMaster-Carr part no. 3190K632) to 31.2 % light viscosity oil (McMaster-Carr part no. 3190K629) ratio. Further details about the implementation of tomo PIV measurements in our TCF apparatus are reported elsewhere (Borrero-Echeverry 2014).

Fully resolved direct numerical simulations (DNS) of TCF were conducted using the code developed by Avila and his collaborators (Avila *et al.* 2008; Mercader, Batiste & Alonso 2010; Avila 2012). This code uses a pseudospectral scheme to solve the Navier–Stokes equation in cylindrical coordinates (r, θ, z) subject to physical (no-slip) boundary conditions at the surface of the rotating concentric cylinders and top and bottom end caps. The geometry of the simulation was chosen to match that of the experimental apparatus. The simulations used $N_r = 20$ Chebyshev modes in the radial direction, $N_z = 100$ Chebyshev modes in the axial direction and $N_\theta = 1280$ Fourier modes in the azimuthal direction, so that the velocity field $\boldsymbol{v}$ at a point (r, θ, z) and time t is given by

$$\boldsymbol{v}(r, \theta, z, t) = \mathrm{Re} \sum_{k=0}^{N_r} \sum_{n=0}^{N_z} \sum_{m=0}^{N_\theta/2} \boldsymbol{V}^{knm}(t) T_k(x) T_n(y) \mathrm{e}^{\mathrm{i}m\theta}, \tag{2.1}$$

where $x = (2r - r_i - r_o)/d$, $y = 2z/h - 1$ (where $0 < z < h$) and $T_n(\cdot)$ is the Chebyshev polynomial of order n. All experimental and numerical results are non-dimensionalized in terms of a characteristic length scale $d = r_o - r_i = 7.64$ mm (the annular gap width) and a characteristic (viscous) time scale $\tau = d^2/\nu = 56.7$ s.

To quantify flow fields in both simulations and experiments, the perturbation flow field

$$\widetilde{\boldsymbol{v}}(t) = \boldsymbol{v}(t) - \boldsymbol{v}^{lam}, \tag{2.2}$$

characterizes the deviation of the full flow $\boldsymbol{v}(t)$ from an axially symmetric laminar flow $\boldsymbol{v}^{lam}$ computed numerically at the same Reynolds numbers. The numerically computed $\boldsymbol{v}^{lam}$ was used to compute the perturbation flow field for both simulations and experiments since the laminar flow is unstable for some Re_i considered in this study, and, therefore, unobservable in the laboratory experiments.

3. Results

First, we briefly describe a coarse experimental exploration of laminar–turbulent (turbulent–laminar) transitions that occur as Re_i is slowly increased (decreased) while maintaining Re_o fixed in the counter-rotating regime. We then focus on the case of $Re_o = -1000$ and examine in detail the transitions associated with increasing and decreasing Re_i using both laboratory experiments and numerical simulations.

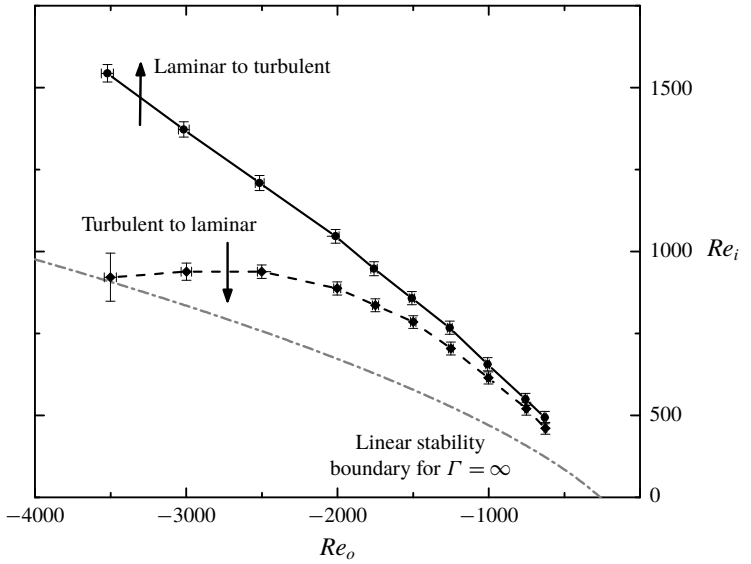

FIGURE 2. Phase diagram illustrating the hysteretic laminar–turbulent transition in experiments on counter-rotating ($Re_o < 0$ and $Re_i > 0$) Taylor–Couette flow with $\Gamma = 5.26$ and $\eta = 0.905$. The diagram indicates transitions observed in experiments where Re_i was increased or decreased quasi-statically while keeping Re_o fixed. The black solid and dashed lines, drawn to guide the eye, indicate the transition boundaries from laminar flow to turbulence and from turbulence to laminar flow, respectively. The grey dash-dotted line represents the marginal stability curve for TCF at $\eta = 0.9$ for $\Gamma = \infty$ (Esser & Grossmann 1996).

3.1. *Laminar–turbulent transition: dependence on Re_o*

To coarsely map out the transition boundaries for TCF in the geometry studied here, we performed flow visualization experiments by first spinning up the outer cylinder from rest (with the inner cylinder stationary) to a specific value of Re_o; then, with Re_o held constant, Re_i was increased in steps of $\Delta Re_i = 10$ by slowly stepping up the rotation rate of the inner cylinder until a qualitative change in the flow was observed. We waited a time interval of 3.2τ between steps to ensure that the flow had reached equilibrium. The turbulent–laminar transition boundary at the same Re_o was then determined by starting in the turbulent regime and slowing the inner cylinder down by $\Delta Re_i = 10$ every 3.2τ until the flow was observed to be in the laminar state. The experiments were repeated for different fixed values of Re_o.

The experimental studies revealed that instability of the azimuthally symmetric smooth laminar flow always leads to turbulence over a range of Re_o from -3500 to -500 (figure 2). The transition back to laminar flow was always observed to be hysteretic with the range in Re_i over which hysteresis occurs increasing as the magnitude of Re_o increases. Our results indicate that transition from laminar flow is suppressed by the moderate aspect ratio of our apparatus, i.e. for fixed Re_o, the transition occurs at Re_i larger than that predicted by linear stability analysis with $\Gamma = \infty$ (grey line in figure 2). This observation is consistent with earlier experiments at larger values of Γ (and somewhat smaller values of η) where, like our studies, the endcaps rotated with the outer cylinder (Hamill 1995). In that work, the delay of the laminar–turbulent transition was found to increase with decreasing Γ, most likely

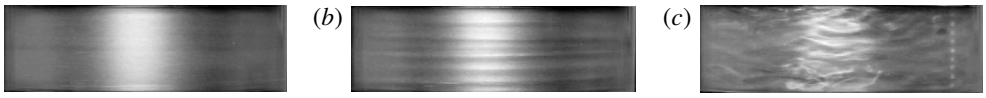

FIGURE 3. Evolution of the flow during laminar to turbulent transition in experiments at $Re_o = -1000$ and $Re_i = 643$. The sequence of snapshots shows (*a*) the initial laminar flow, (*b*) transient interpenetrating spirals and (*c*) persistent intermittent turbulence.

due to the endwall effects (e.g. dissipation and Ekman pumping) that become more pronounced as Γ decreases.

3.2. *Flow transitions at* $Re_o = -1000$

A detailed experimental and numerical investigation at fixed $Re_o = -1000$ led to the observation of an intermediate state that plays an important role in the laminar–turbulent transition. The transition from turbulence to laminar flow was found to involve an aperiodic stable intermediate state (interpenetrating spirals) that persists over a range of Re_i. Moreover, IPS were found to appear – albeit transiently – during the transition from laminar flow to turbulence. Transitions between different flow states are described in detail below.

3.2.1. *Transitions in laboratory experiments*

Transitions were determined in flow visualization studies by first spinning up the outer cylinder to $Re_o = -1000$ (with the inner cylinder at rest), and then increasing the inner cylinder's counter-rotation in steps of $\Delta Re_i = 0.5$ every 3.2τ, until the flow became turbulent. Subsequently, beginning from the turbulent state, Re_i was decreased at the same rate as before until the flow returned to the laminar state. No observable shifts in the transition boundaries were found when incrementing or decrementing Re_i in steps of $\Delta Re_i = 0.25$ separated in time by 10.7τ.

With the flow starting in a laminar state, laboratory experiments exhibit a laminar–turbulent transition at $Re_i = 643$ with a total uncertainty in Re_i of ± 2. Repeated measurements demonstrate the transition can be observed with a resolution of ± 0.13 (i.e. 0.02 %), as constrained by the mechanical limits of the motor and transmission driving the inner cylinder; in other words, from laminar flow just below threshold (cf. figure 3*a*), a single increment of $\Delta Re_i = 0.13$ results in turbulence. At onset (with Re_i fixed), the structure of the flow changes slowly at first; very weak interpenetrating spirals gradually become discernible and grow slowly in amplitude with time (cf. figure 3*b*). Then, abruptly, the spirals break up and spatio-temporally intermittent turbulence develops on top of an IPS-like background flow and persists (cf. figure 3*c*). The interval of time over which the flow resembles IPS before transitioning to turbulence was different each time the experiment was performed and this interval decreased with an increase in the increment size of ΔRe_i. If Re_i is increased stepwise (with a fixed time interval of 3.2τ between each step), the transition Re_i is unchanged for increments of $\Delta Re_i < 1$; the transition Re_i is observed to decrease for increments of $\Delta Re_i > 1$.

Starting from turbulent flow, decreasing Re_i reveals a transition to stable IPS at $Re_i = 625 \pm 3.6$. IPS were observed to be weakly chaotic (i.e. having a broad-band temporal spectrum) over a range of Re_i and persist for as long as $3.8 \times 10^3 \tau$ (two and a half days, after which time the experiments were ended). From stable IPS, increasing Re_i leads to a transition back to intermittent turbulence at $Re_i = 631 \pm 3.7$; decreasing

Transition	Experiment	Noiseless DNS
Laminar → turbulence	643 ± 2	675 ± 5
Turbulence → IPS	625 ± 3.6	623.5 ± 0.5
IPS → turbulence	631 ± 3.7	630.5 ± 0.5
IPS → laminar	617 ± 1	617.5 ± 0.5

TABLE 1. The inner cylinder Reynolds numbers for flow transitions are shown for both laboratory experiments and numerical simulations at $Re_o = -1000$. Uncertainty values from the experiment reflect the systematic uncertainties associated with the measurement of Re as well as repeatability of the transition, while the uncertainty values from the noiseless DNS reflect the resolution with which the dependence on Re_i was investigated. The uncertainties in experimental values were calculated using an uncorrelated linear propagation of uncertainties associated with all measured quantities and measurement repeatability represented by the standard deviation.

Re_i leads instead to a transition to the axisymmetric laminar state at $Re_i = 617 \pm 1$. It should be noted that the values of Re_i at which various transitions are observed (see table 1) depend on disturbances of two qualitatively different types: (a) disturbances associated with a discrete change of Re_i and (b) other types of disturbances (e.g. the cylinders not being perfectly round or coaxial, the deviation in their angular velocity from a constant, etc.). All of these are disturbances of a finite, although likely small, amplitude.

Quenching experiments can provide information on the transition from chaotic/turbulent states that is complementary to results obtained via quasi-static changes in Reynolds number (Bottin & Chaté 1998; Prigent & Dauchot 2005; Peixinho & Mullin 2006; Borrero-Echeverry *et al.* 2010). A typical quenching experiment begins with the flow in a chaotic/turbulent state at fixed Reynolds numbers. At an instant in time, Re_i is abruptly increased or decreased to a new value and held constant; the subsequent 'lifetime' of the flow (the time required for the initial flow to change to a qualitatively different state) is determined. Repeating the same experiment often yields a distribution of measured lifetimes, which provides insight into the nature of the transition. To probe the transition from turbulence to IPS, a turbulent state at $Re_i = 640$ was first established and monitored for 5.3τ; the inner cylinder rotation was then rapidly (in approximately $4.2 \times 10^{-3}\tau$) reduced to $Re_i = 623$. The time interval between the reduction in Re_i and the disappearance of turbulence was recorded. Similarly, to probe the transition from IPS to turbulence, we initially set $Re_i = 623$. The IPS was monitored for 5.3τ; then, the inner cylinder rotation was rapidly (in approximately $4.2 \times 10^{-3}\tau$) increased to $Re_i = 640$ and the time interval between the increase in Re_i and the first appearance of turbulence was recorded.

Figure 4 summarizes the results from 250 experiments performing the same cycle of transitions between turbulence and IPS; the data indicate a clear exponential distribution of intervals between the time when the inner cylinder rotation rate is changed and the time at which turbulence either completely disappears (cf. figure 4*a*) or first appears (cf. figure 4*b*). The exponential distribution suggests that both transitions describe a memoryless Poisson process, with a chaotic attractor at the initial Re_i becoming a chaotic repeller at the final Re_i. There are, however, different scenarios that could gives rise to exponential distribution of transition times such as a boundary crisis bifurcation (Kadanoff & Tang 1984; Kantz & Grassberger 1985) and a noise-induced transition (Do & Lai 2005); to determine the specific

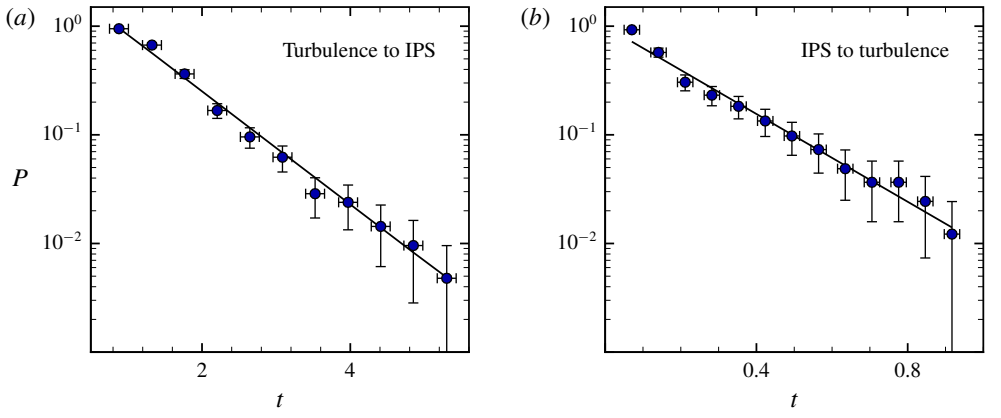

FIGURE 4. Transition probability $P(t)$. After an abrupt change in Re_i, the transition time for turbulence to either (*a*) disappear or (*b*) first appear is exponentially distributed. $P(t)$ indicates the fraction of experimental trials where either (*a*) turbulence still persists after changing Re_i from 640 to 623 or (*b*) turbulence has not yet appeared after changing Re_i from 623 to 640. The uncertainty bars in the vertical direction describe the uncertainty $U_P = \sqrt{f(1-f)/N}$, where $f(t)$ is the fraction of the number of events where turbulence survived for longer than time t and N is the total number of events observed (Moore & McCabe 1998).

mechanism at play here, further investigation would be needed. Similar distributions of transition lifetimes were found in relaminarization studies of high-aspect-ratio TCF (Borrero-Echeverry *et al.* 2010).

Quenching experiments were also performed for the transition from stable IPS to laminar flow; however, due to the discreteness with which Re_i could be varied in experiment, we could not find a final Re_i for which a meaningful distribution of lifetimes could be observed.

3.2.2. *Transitions in numerical simulations*

Numerical simulations were used to determine linear stability of the steady axisymmetric laminar flow $\boldsymbol{v}^{lam}$. This flow was generated at $Re_o = -1000$ and different fixed Re_i by keeping only the $m = 0$ azimuthal Fourier mode and evolving the state until it stopped changing. The azimuthal symmetry of this flow was then broken by perturbing the $m = 1$ Fourier mode (with the nonlinear term generating disturbances for all $m \neq 0$). Specifically, a random Gaussian noise with standard deviation $\sigma = 10^{-8}$ was added to the coefficient of each of the spectral modes $\boldsymbol{V}_i^{kn1}|_{t=0}$, $i = r, \theta, z$ (note this is a very small perturbation since $\boldsymbol{V}_\theta^{kn0} = O(Re_o)$). Evolving the perturbed flow, we found that the perturbation decays (the laminar state is linearly stable) for $Re_i < Re_i^c = 675 \pm 5$ and grows, resulting in a transition to turbulence, for $Re_i > Re_i^c$.

Since the laminar flow undergoes transition to turbulence in experiment at a notably lower Re_i than the linear stability threshold Re_i^c, an investigation of its stability to finite amplitude disturbances was performed. Qualitatively, we find that, for $Re_i \geqslant 634$, finite amplitude perturbations lead to destabilization of the laminar state (cf. figure 5*a*), giving rise to IPS with an amplitude that grows and saturates temporarily (cf. figure 5*b*). Ultimately the IPS gives way to spatio-temporally intermittent turbulence (cf. figure 5*c*), just as in the experiment. Qualitatively the same transition sequence

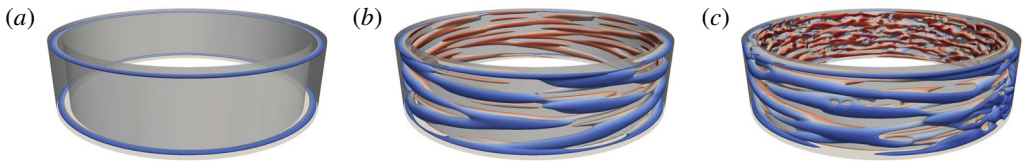

FIGURE 5. Evolution of the flow during the laminar to turbulent transition in numerical simulations at $Re_o = -1000$ and $Re_i = 645$. (*a*) A laminar flow becomes unstable, transitioning first to (*b*) interpenetrating spirals and, eventually, (*c*) turbulence. Each panel shows isosurfaces of the radial velocity component; the colour indicates the corresponding azimuthal velocity component. Red (blue) indicates flow in the same direction as the inner (outer) cylinder rotation.

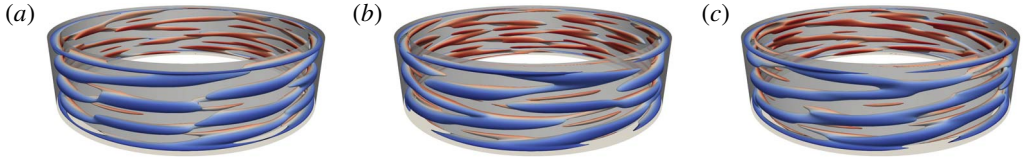

FIGURE 6. Interpenetrating spirals at $Re_o = -1000$ and (*a*) $Re_i = 620$, (*b*) $Re_i = 625$, (*c*) $Re_i = 630$. Each panel shows isosurfaces of the radial velocity component; the colour indicates the corresponding azimuthal velocity component. Red (blue) indicates flow in the same direction as the inner (outer) cylinder rotation.

was found to occur for initial disturbances with different magnitudes and spatial profiles.

To quantify qualitatively how the critical disturbance amplitude depends on Re_i, we fixed the spatial profile of the disturbance by choosing the initial condition in the form of a homotopy

$$\boldsymbol{v} = (1-\alpha)\boldsymbol{v}^{lam} + \alpha \boldsymbol{v}^{IPS}, \tag{3.1}$$

where $\boldsymbol{v}^{lam}$ is the laminar flow at the given Re_i and $\boldsymbol{v}^{IPS}$ is a snapshot of the (non-axisymmetric) IPS at $Re_i = 630$. As figure 6 illustrates, the structure of the IPS is fairly similar at different Re_i; thus, for the purpose of determining critical disturbance amplitudes, we considered it to be sufficient to compute $\boldsymbol{v}^{IPS}$ at a fixed Re_i. The homotopy parameter $0 \leqslant \alpha \leqslant 1$ characterizes the magnitude of the disturbance; increasing α increases the disturbance amplitude. This particular choice of homotopy guarantees that initial conditions are divergence free for any value of α.

For each Re_i we considered, a series of numerical simulations were performed with each simulation at a different value of α; the simulations were run until the flow approached an asymptotic state. We then used bisection to determine the largest value of α at which the flow relaminarized. The critical value α_c is then defined as the midpoint between the two α values found that produce relaminarization and transition. The results are summarized in figure 7 and suggest that the bifurcation at Re_i^c leading to the loss of stability of the laminar flow is subcritical, with α_c decreasing with increasing Re_i and vanishing at Re_i^c. Furthermore, for $Re_i \geqslant 634$, disturbances with $\alpha > \alpha_c$ lead to a transition to turbulence with IPS serving as a transient intermediate state. For $Re_i \leqslant 633$, on the other hand, disturbances with $\alpha > \alpha_c$ lead to a transition to stable IPS. We note that the value $Re_i = 643 \pm 2$ at which the transition to turbulence

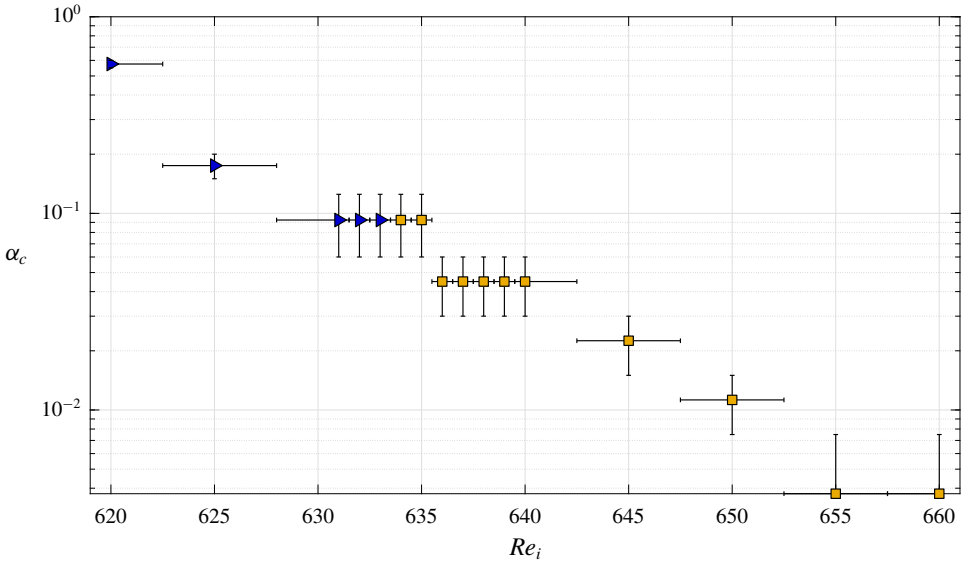

FIGURE 7. The critical magnitude α_c of the homotopy parameter below which the flow relaminarizes at different Re_i. The symbols ▶ and ■ denote that the flows at this Re_i transition to IPS and turbulence, respectively, for $\alpha > \alpha_c$.

is found in experiment corresponds to $\alpha_c \approx 0.02$, suggesting the ambient disturbance level present in the experiments is fairly low.

To illustrate the transition from laminar flow to turbulence, figure 8 shows the energies of the ten leading azimuthal Fourier modes ($m = 0, \ldots, 9$)

$$E_m(t) = \int_{\eta/(1-\eta)}^{1/(1-\eta)} r\,\mathrm{d}r \int_0^{\Gamma} |\boldsymbol{v}_m(t)|^2\,\mathrm{d}z, \tag{3.2}$$

where $\boldsymbol{v}_m$ is the mth Fourier component of the velocity field, for a representative numerical simulation at $Re_i = 640$, where the initial condition was constructed using the homotopy (3.1) with $\alpha = 0.06$. One can clearly see three distinct regimes: for $0 < t \lessapprox 0.7$ the perturbation about the laminar flow grows. For $0.7 \lessapprox t \lessapprox 1.6$, the flow temporarily saturates into IPS where the mode energies remain roughly constant, with modes $m = 4$ and $m = 5$ dominating. Finally, for $t \gtrapprox 1.6$, IPS give way to turbulence. The flows corresponding to the three regimes are qualitatively similar to those shown in figure 5.

Note that our findings are consistent with the related numerical study performed by Meseguer *et al.* (2009*b*) for a counter-rotating Taylor–Couette flow with comparable η, Re_i, and Re_o, but axially periodic boundary conditions. In that study, travelling wave states featuring spiral flows were found to arise in a subcritical bifurcation of the laminar flow, with the modes $m = 4$ and $m = 5$ destabilizing at the lowest Re_i. This raises the possibility that the unstable travelling wave(s) corresponding to these modes serve as the 'edge states' whose stable manifold(s) serve as the boundary between the laminar flow and chaotic IPS (Schneider *et al.* 2008). The data presented in figures 7 and 8 are certainly consistent with this possibility.

Numerical simulations find the same sequence of transitions as laboratory experiments when the flow is initially turbulent. Decreasing Re_i first leads to a

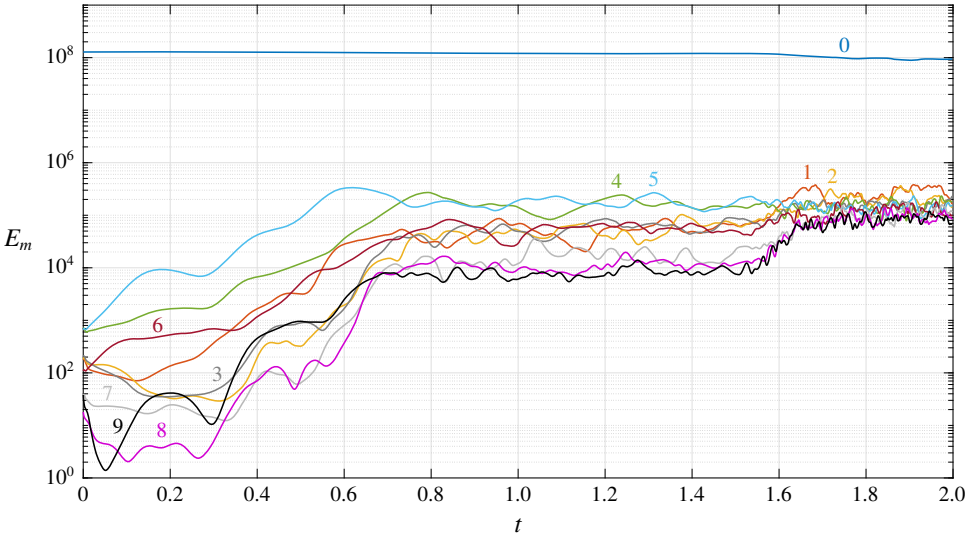

FIGURE 8. The energy of the flow contained in the ten leading azimuthal Fourier modes during the transition from laminar flow to turbulence at $Re_i = 640$. The mode numbers are shown next to each curve.

transition to stable IPS at $Re_i = 623.5 \pm 0.5$. From stable IPS, increasing Re_i leads to a transition back to turbulence at $Re_i = 630.5 \pm 0.5$, while decreasing Re_i leads to a transition to the time-independent laminar state at $Re_i = 617.5 \pm 0.5$. These numerically determined transition Reynolds numbers between IPS and turbulence and from IPS to laminar are quantitatively in agreement with those found in laboratory experiments, as illustrated in table 1. However, due to the subcritical nature of the transition between laminar and turbulent flow, an appropriate choice of finite amplitude perturbation is required to properly compare the transition thresholds in experiment and numerics.

The protocol for determining Re_i for transition from turbulence to IPS is as follows: we started with verifying that turbulence persists at $Re_i = 640$ by evolving the flow for a time interval 5.264τ. Then we ramped down Re_i in increments of $\Delta Re_i = 5$ and evolved the flow for the same interval to determine whether a transition occurred. Once a transition was detected (at $Re_i = 620$), we re-initialized the flow using the final state of the simulation at $Re_i = 625$, decreased the Reynolds number by $\Delta Re_i = 1$, and evolved the flow for a further 5.264τ. The procedure was repeated with $\Delta Re_i = 2, 3, \ldots$ until a transition was found.

A similar protocol was used for the two transitions from stable IPS. In these cases, we verified that stable IPS persists at $Re_i = 620$ and 630. The final states of the simulation at $Re_i = 630$ (or $Re_i = 620$) were evolved for 5.264τ at a fixed Re_i that was increased (or decreased) by $\Delta Re_i = 1, 2, 3, \ldots$ until transition to turbulence (or laminar flow) was found. Note that, in all of these cases, only one simulation was performed and the finest resolution was $\Delta Re_i = 1$, which determines the accuracy of the values reported in table 1.

Given ample experimental evidence that the transitions between turbulence and IPS are probabilistic, we did not investigate these transitions numerically in more detail. For the transition from IPS to laminar flow, however, experiments did not conclusively determine the nature of the transition. We therefore performed an additional numerical investigation of this transition by evolving IPS at a number of

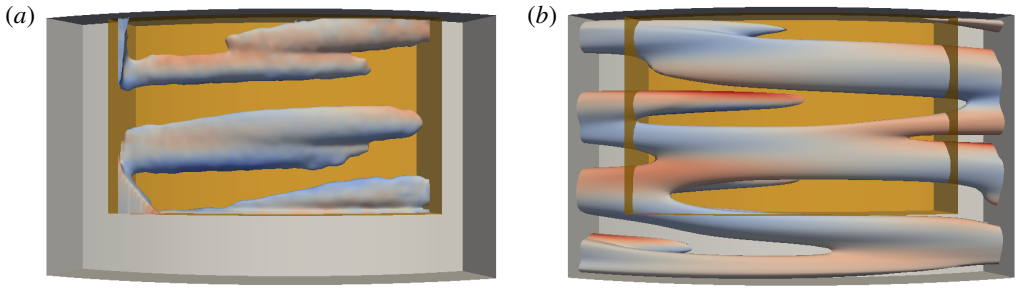

FIGURE 9. A snapshot of interpenetrating spirals in (*a*) a tomo PIV experiment and (*b*) DNS. Each image shows a single isosurface of the perturbation field, $\widetilde{\boldsymbol{v}}_\theta$, for $Re_i = 625$ and $Re_o = -1000$ inside a cylindrical subvolume. The colour indicates the corresponding azimuthal velocity component. Red (blue) indicates flow in the same direction as the inner (outer) cylinder rotation. The shaded orange rectangular box represents the region probed by tomo PIV, which spans approximately 10 % of the flow domain volume.

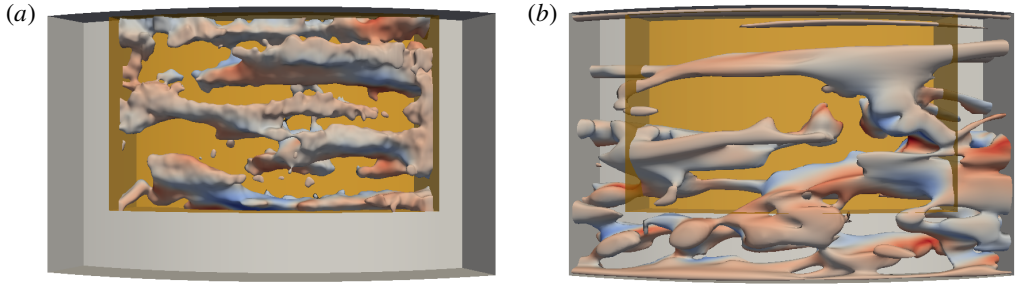

FIGURE 10. A snapshot of a turbulent flow in experiment (*a*) and DNS (*b*). Each image shows a single isosurface of the perturbation field, $\widetilde{\boldsymbol{v}}_\theta$, for $Re_i = 650$ and $Re_o = -1000$ inside a cylindrical subvolume. The colour indicates the corresponding azimuthal velocity component. Red (blue) indicates flow in the same direction as the inner (outer) cylinder rotation. The shaded orange rectangular box represents the region probed by tomo PIV, which spans approximately 10 % of the flow domain volume.

fixed Re_i in the range (617, 618). While most of the results were consistent with a transition threshold found previously, there were a few outliers. In particular, we found that evolving IPS for 5.264τ at $Re_i = 617.8125$ does not result in a transition to a laminar flow, although eventually the flow does relaminarize. This result shows that the transition from IPS to laminar flow also appears to have a probabilistic nature and does not correspond to a bifurcation which would have resulted in a sharp transition boundary.

3.2.3. *Flow field characterization*

Flow fields computed numerically also compare well with measurements from laboratory experiments. The stable IPS found in simulations and experiments exhibit a similar spatial structure (figure 9). Moreover, both experiments and simulations show that just above the onset of turbulence, the flow features localized patches of turbulence that co-exist with disordered spiral structures (cf. figures 5*c* and 10). To quantitatively compare the flows in experiment and numerics, we computed the average energy E corresponding to the θ component of the velocity perturbation

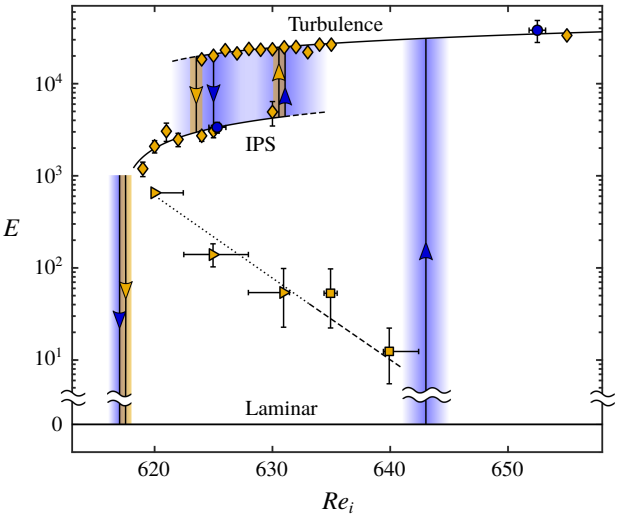

FIGURE 11. Transition map for the three flow states: laminar, IPS and turbulence. Numerically computed values of E for stable IPS and turbulence at various Re_i are plotted as ◆ while the values calculated from experimental measurements are plotted as ●. The gold and blue arrows indicate the values of Re_i at which transitions occur in simulation and experiment respectively. The shading around the arrows corresponds to the uncertainty in the transitional Re_i value. The ▶ and ■ symbols represent the E value associated with the critical magnitude of the finite amplitude perturbation considered here, which corresponds to $\alpha = \alpha_c$, necessary to initiate transition from laminar flow to IPS and turbulence, respectively. All curves are to guide the eye only.

$\widetilde{\boldsymbol{v}} = \boldsymbol{v} - \boldsymbol{v}^{lam}$ over a time interval $T = O(\tau)$ and region Ω in the r, z plane at a fixed azimuthal location where experimental velocity measurements were available. Only the θ-component of velocity was analysed because v_r and v_z had increased noise due to the frame rates used in the PIV. The region Ω is bounded by the coordinates $r \in [\eta/(1-\eta),\ 1/(1-\eta)]$ and $z/\Gamma \in [0.254,\ 0.973]$, where z is measured from the bottom of the flow domain. For the stable states (IPS and turbulence), the average energy was defined according to

$$E = \frac{1}{TA} \int_0^T \mathrm{d}t \int_\Omega \widetilde{v}_\theta^2(t)\, \mathrm{d}r\, \mathrm{d}z, \tag{3.3}$$

where A is the area of the cross-section of Ω.

The information presented in previous sections is summarized in figure 11 in the form of a bifurcation diagram. In particular, we find that the energy E serves as a good order parameter that allows one to easily distinguish the qualitatively different flows (laminar flow, IPS and turbulence) and to determine where transitions between different flows take place. In particular, we find that the average values of E in experiment and numerics are in good quantitative agreement and that E changes smoothly with Re_i for both IPS and turbulent flow over the regions where these flows are stable (indicated by solid black lines). The dashed lines indicate the trends when these flow states become unstable and are merely extrapolations of the solid curves.

The figure also shows how the energy of the critical disturbance that lies on the boundary of the basin of attraction of the stable laminar flow varies with Re_i.

The dotted (dashed) line denotes to the transition to IPS (turbulence). To compute this boundary, we performed the average over the azimuthal variable rather than time in (3.3), where $\widetilde{\boldsymbol{v}} = \alpha(\boldsymbol{v}^{IPS} - \boldsymbol{v}^{lam})$ according to (3.1) and $\alpha = \alpha_c$. Although the specific values of E which define this boundary, just like α_c, depend on the spatial structure of the perturbation $\widetilde{\boldsymbol{v}}$, the shape of the boundary suggests that it is related to an unstable edge state (or states) connecting the laminar state and IPS, as discussed previously.

4. Discussion

Two distinct instabilities at play in counter-rotating TCF form the basis for a qualitative physical picture of turbulent transition. In the limiting case where Re_o approaches zero (the outer cylinder is at rest), the laminar flow is subject to centrifugal instability when Re_i is sufficiently large. By contrast, in the limiting case where Re_i approaches zero (the inner cylinder is at rest), the flow is centrifugally stable for all values of Re_o, but is subject to shear instability for Re_o sufficiently large. Under counter-rotation, both instability mechanisms can, roughly speaking, be thought of as operative in distinct spatial regions, separated by a 'nodal surface' where the azimuthal velocity component is zero. On the side of the nodal surface nearer the inner cylinder, the azimuthal velocity component is decreasing with increasing radial distance from the inner cylinder, thereby providing a necessary condition for centrifugal instability in this (inner) flow region. On the side of the nodal surface nearer the outer cylinder, centrifugal instability is ruled out since the azimuthal velocity component is increasing with increasing radial distance from the inner cylinder; however, shear flow instabilities remain a possibility in this (outer) flow region.

Prior work in large-aspect-ratio counter-rotating TCF has described a scenario in which the interplay between the inner and outer flow regions leads to turbulent transition. When Re_o is fixed and sufficiently large in magnitude and Re_i is increased quasi-statically, the primary instability of the laminar flow leads to the formation of stable spiral flows (Coles 1967; Andereck *et al.* 1986; Eckhardt & Yao 1995; Goharzadeh & Mutabazi 2001), which are mainly confined to the centrifugally unstable inner region and qualitatively similar to IPS described in the present paper. Simulations with periodic axial boundary conditions (Coughlin & Marcus 1996) showed that, as Re_i is increased beyond the primary instability, the spiral flow in the inner region increasingly disturbs the centrifugally stable outer region. Coughlin & Marcus found that, beyond a certain Re_i, the disturbance amplitude becomes strong enough to trigger a shear instability in the outer layer leading to turbulence. This transition scenario is in qualitative agreement with experimental observation in TCF with moderate-to-large aspect ratios ($17 \leqslant \Gamma \leqslant 46$) (Hamill 1995).

Our experimental results suggest the interactions between inner and outer flow regions also play a central role in transition in small-aspect-ratio TCF, with the important difference that transition from laminar flow leads directly to turbulence facilitated by the temporary appearance of IPS. The laminar state with Re_o fixed exhibits a subcritical rather than a supercritical instability as Re_i increased quasi-statically. Consequently, as Re_i increases, the laminar flow undergoes a finite amplitude instability leading to growth of a spiral flow mostly confined to the inner region (cf. figure 12*a*). However, unlike the large-aspect-ratio case, the emerging spiral states are transient, with the flow in the inner region generating disturbances of sufficient amplitude to trigger shear instability in the outer region leading to

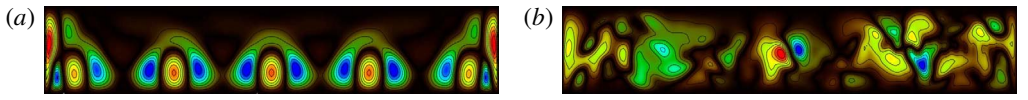

FIGURE 12. Typical snapshots of the radial velocity in the constant θ plane for (a) IPS and (b) turbulence in the numerical simulation at $Re_i = 637$ and $Re_o = -1000$. The r direction is vertical and z is horizontal, with the inner cylinder at the bottom. Red (blue) indicates positive (negative) values of v_r.

turbulence (cf. figure 12b). Stable IPS do exist in our system at lower Re_i, but are disconnected from the axisymmetric laminar solution. The transition from stable IPS to turbulence appears similar to the large-aspect-ratio case.

This transition, as well as the reverse transition from turbulence to stable IPS are similar from a dynamical systems standpoint. The results shown in figure 4(a) for the decay from turbulence is reminiscent of earlier observations of transitions from turbulence in pipe flows (Faisst & Eckhardt 2004; Peixinho & Mullin 2006; Avila *et al.* 2011) and in large-aspect-ratio TCF driven solely by outer cylinder rotation (Borrero-Echeverry *et al.* 2010). In all these cases, the exponential decay from turbulence is suggestive of a memoryless process in which, from a state space viewpoint, the transient character of turbulence is captured by a finite-time escape from a chaotic repeller to a qualitatively different solution. Interestingly, in all previous work, once the turbulent transients had disappeared, the flow relaminarized; by contrast, our results demonstrate, for the first time, that turbulence gives way to another chaotic state (IPS). Moreover, figure 4(b) suggests the transition from IPS to turbulence exhibits a similar character, so that for sufficiently large Re_i, IPS are described by a chaotic repeller and the flow transitions to a different chaotic state (turbulence). In this regard, the origin of the IPS-to-turbulent transition observed here is quite different from the linear secondary instability mechanism proposed earlier (Coughlin & Marcus 1996). The change of the nature of the chaotic set underlying IPS from an attractor at lower Re_i to a repeller at higher Re_i also explains the transient appearance of IPS during the transition from laminar to turbulent flow.

Prior work has demonstrated the chaotic behaviour of IPS arises from competition between spiral modes of different wavenumbers and helicities (Andereck *et al.* 1986; Hamill 1995; Coughlin & Marcus 1996). Our observations of IPS were made in a TCF apparatus with an aspect ratio substantially smaller than that employed in earlier studies of IPS; thus, axial confinement effects in our work hinders clear identification of distinct spiral modes at play in IPS. Nevertheless, we speculate that chaos in IPS observed here originates from qualitatively similar mode interactions as that found in larger-aspect-ratio studies.

5. Conclusion

Our experimental and numerical results indicate that, for suitable parameter values, Taylor–Couette flow can exhibit some key characteristics commonly observed in the transition to turbulence in other shear flows. The transition from laminar flow to turbulence is subcritical, like that observed for flows in channels and boundary layers. In particular, when transition is probed by increasing Re_i sufficiently slowly (see § 3.2.1), structured, non-turbulent flows (transient interpenetrating sprials) mediate the transition to turbulence in Taylor–Couette flow in a manner that is analogous to the role of Tollmien–Schlichting (TS) waves in the transition to turbulence in channels

and boundary layers in low-noise environments. However, there are also significant differences between Taylor–Couette flow and other canonical shear flows: the physical instability mechanism of IPS (centrifugal instability) differs from the mechanisms for TS waves; TCF transition does not feature a linear growth regime like that found for TS waves in channel and boundary layer transition; stable, nonlinearly saturated TS waves are never observed in channels/boundary layers, unlike the stable IPS observed in TCF.

Subcritical laminar–turbulent transition is most commonly studied in open flows. However, closed flows such as TCF, which display highly reproducible transitions and close correspondence between numerics and experiments, offer opportunities to explore in much greater detail behaviours that may show up in a variety of shear flows, open or closed. One such opportunity for future study emerging from recent theoretical and experimental work suggests that the dynamics of turbulent flows is guided by particular unstable solutions to the Navier–Stokes equation (Hof *et al.* 2004; Suri *et al.* 2017). This work suggests that selected solutions with simple temporal behaviour (e.g. equilibria, limit cycle oscillations) exhibit spatial structures that are strikingly similar to well-known patterns (coherent structures) that have long been known to play a central role in turbulence; moreover, a suitable selection of such solutions (known as exact coherent structures) can be harnessed to capture turbulent flow dynamics and statistics (e.g. average turbulent flow properties). Our results suggest that exact coherent structures with spiral spatial structures could play a role in mediating laminar–turbulent transition in counter-rotating Taylor–Couette flow.

Acknowledgements

The authors would like to acknowledge the financial support by the Army Research Office under grant nos W911NF-15-10471 and W911NF-16-10281. D.B.-E. gratefully acknowledges the support of the M. J. Murdock Charitable Trust (Award no. 2015214) and the Kresge Endowment at Willamette University. We are grateful to M. Avila for sharing the Taylor–Couette DNS solver used here with us and for many useful discussions.

Declaration of interests

The authors report no conflict of interest.

REFERENCES

ANDERECK, C. D., LIU, S. S. & SWINNEY, H. L. 1986 Flow regimes in a circular Couette system with independently rotating cylinders. *J. Fluid Mech.* **164**, 155–183.

AVILA, K. & HOF, B. 2013 High-precision Taylor–Couette experiment to study subcritical transitions and the role of boundary conditions and size effects. *Rev. Sci. Instrum.* **84**, 065106.

AVILA, K., MOXEY, D., DE LOZAR, A., AVILA, M., BARKLEY, D. & HOF, B. 2011 The onset of turbulence in pipe flow. *Science* **333**, 192–196.

AVILA, M. 2012 Stability and angular-momentum transport of fluid flows between corotating cylinders. *Phys. Rev. Lett.* **108**, 124501.

AVILA, M., GRIMES, M., LOPEZ, J. M. & MARQUES, F. 2008 Global endwall effects on centrifugally stable flows. *Phys. Fluids* **20**, 104104.

BORRERO-ECHEVERRY, D. 2014 Subcritical transition to turbulence in Taylor–Couette flow. PhD thesis, Georgia Institute of Technology.

BORRERO-ECHEVERRY, D., CROWLEY, C. J. & RIDDICK, T. P. 2018 Rheoscopic fluids in a post-Kalliroscope world. *Phys. Fluids* **30**, 087103.

BORRERO-ECHEVERRY, D. & MORRISON, B. C. A. 2016 Aqueous ammonium thiocyanate solutions as refractive index-matching fluids with low density and viscosity. *Exp. Fluids* **57**, 123.

BORRERO-ECHEVERRY, D., SCHATZ, M. F. & TAGG, R. 2010 Transient turbulence in Taylor–Couette flow. *Phys. Rev.* E **81**, 025301(R).

BOTTIN, S. & CHATÉ, H. 1998 Statistical analysis of the transition to turbulence in plane Couette flow. *Eur. Phys. J.* B **6**, 143–155.

BURIN, M. J. & CZARNOCKI, C. J. 2012 Subcritical transition and spiral turbulence in circular Couette flow. *J. Fluid Mech.* **709**, 106–122.

COLES, D. 1965 Transition in circular Couette flow. *J. Fluid Mech.* **21**, 385–425.

COLES, D. 1967 A note on Taylor instability in circular Couette flow. *Trans. ASME J. Appl. Mech.* **34**, 529–534.

COUETTE, M. M. 1890 Études sur le frottement des liquides. *Ann. Chim. Phys.* **20**, 433–510.

COUGHLIN, K. & MARCUS, P. S. 1996 Turbulent bursts in Couette–Taylor flow. *Phys. Rev. Lett.* **77**, 2214.

DO, Y. & LAI, Y.-C. 2005 Scaling laws for noise-induced superpersistent chaotic transients. *Phys. Rev.* E **71**, 046208.

ECKHARDT, B. & YAO, D. 1995 Local stability analysis along Lagrangian paths. *Chaos, Solitons and Fractals* **5**, 2073–2088.

EDLUND, E. M. & JI, H. 2014 Nonlinear stability of laboratory quasi-Keplerian flows. *Phys. Rev.* E **89**, 021004(R).

ELSINGA, G. E., SCARANO, F., WIENEKE, B. & VAN OUDHEUSDEN, B. W. 2006 Tomographic particle image velocimetry. *Exp. Fluids* **41**, 933–947.

ESSER, A. & GROSSMANN, S. 1996 Analytic expression for Taylor–Couette stability boundary. *Phys. Fluids* **8**, 1814–1819.

FAISST, H. & ECKHARDT, B. 2004 Sensitive dependence on initial conditions in transition to turbulence in pipe flow. *J. Fluid Mech.* **504**, 343–352.

GOHARZADEH, A. & MUTABAZI, I. 2001 Experimental characterization of intermittency regimes in the Couette–Taylor system. *Eur. Phys. J.* B **19**, 157–162.

HAMILL, C. F. 1995 Turbulent bursting in the Couette–Taylor system. Master's thesis, University of Texas at Austin.

HOF, B., VAN DOORNE, C. W. H., WESTERWEEL, J., NIEUWSTADT, F. T. M., FAISST, H., ECKHARDT, B., WEDIN, H., KERSWELL, R. R. & WALEFFE, F. 2004 Experimental observation of nonlinear traveling waves in turbulent pipe flow. *Science* **305**, 1594–1598.

JI, H., BURIN, M., SCHARTMAN, E. & GOODMAN, J. 2006 Hydrodynamic turbulence cannot transport angular momentum effectively in astrophysical disks. *Nature* **444**, 343–346.

KADANOFF, L. P. & TANG, C. 1984 Escape from strange repellers. *Proc. Natl Acad. Sci. USA* **81**, 1276–1279.

KANTZ, H. & GRASSBERGER, P. 1985 Repellers, semi-attractors, and long-lived chaotic transients. *Physica* D **17**, 75–86.

LOPEZ, J. M. 2016 Subcritical instability of finite circular Couette flow with stationary inner cylinder. *J. Fluid Mech.* **793**, 589–611.

LOPEZ, J. M. & MARQUES, F. 2003 Small aspect ratio Taylor–Couette flow: Onset of a very-low-frequency three-torus state. *Phys. Rev.* E **68**, 036302.

MALLOCK, A. 1896 Experiments on fluid viscosity. *Phil. Trans. R. Soc. Lond.* A **1897**, 41–56.

MARETZKE, S., HOF, B. & AVILA, M. 2014 Transient growth in linearly stable Taylor–Couette flows. *J. Fluid Mech.* **742**, 254–290.

MATISSE, P. & GORMAN, M. 1984 Neutrally buoyant anisotropic particles for flow visualization. *Phys. Fluids* **27**, 759.

MERCADER, I., BATISTE, O. & ALONSO, A. 2010 An efficient spectral code for incompressible flows in cylindrical geometries. *Comput. Fluids* **39**, 215–224.

MESEGUER, A., MELLIBOVSKY, F., AVILA, M. & MARQUES, F. 2009*a* Families of subcritical spirals in highly counter-rotating Taylor–Couette flow. *Phys. Rev.* E **79**, 036309.

MESEGUER, A., MELLIBOVSKY, F., AVILA, M. & MARQUES, F. 2009*b* Instability mechanisms and transition scenarios of spiral turbulence in Taylor–Couette flow. *Phys. Rev.* E **80**, 046315.

MOORE, D. & MCCABE, P. G. 1998 *Introduction to the Practice of Statistics*, 3rd edn. W. H. Freeman.

MORKOVIN, M. V. 1985 Bypass transition to turbulence and research desiderata. In *Transition in Turbines* (ed. R. Graham), NASA Conference Publications, vol. 2386, pp. 161–204. NASA Scientific and Technical Information Office.

NISHIOKA, M., IIDA, S. & ICHIKAWA, Y. 1975 An experimental investigation of the stability of plane Poiseuille flow. *J. Fluid Mech.* **72**, 731–751.

PAOLETTI, M. S. & LATHROP, D. P. 2011 Angular momentum transport in turbulent flow between independently rotating cylinders. *Phys. Rev. Lett.* **106**, 024501.

PEIXINHO, J. & MULLIN, T. 2006 Decay of turbulence in pipe flow. *Phys. Rev. Lett.* **96**, 094501.

PFISTER, G., SCHMIDT, H., CLIFFE, K. A. & MULLIN, T. 1988 Bifurcation phenomena in Taylor–Couette flow in a very short annulus. *J. Fluid Mech.* **191**, 1–18.

PRIGENT, A. & DAUCHOT, O. 2005 Transition to versus from turbulence in subcritical Couette flows. In *IUTAM Symposium on Laminar-Turbulent Transition and Finite Amplitude Solutions* (ed. T. Mullin & R. Kerswell), pp. 195–219. Springer.

RESHOTKO, E. 1976 Boundary-layer stability and transition. *Annu. Rev. Fluid Mech.* **8**, 311–349.

RICHARD, D. & ZAHN, J. P. 1999 Turbulence in differentially rotating flows: What can be learned from the Couette–Taylor experiment. *Astronom. Astrophys.* **347**, 734–738.

SCHNEIDER, T. M., GIBSON, J. F., LAGHA, M., DE LILLO, F. & ECKHARDT, B. 2008 Laminar-turbulent boundary in plane Couette flow. *Phys. Rev.* E **78** (3), 037301.

SCHULTZ-GRUNOW, F. 1959 Zur Stabilität der Couette–Strömung. *Z. Angew. Math. Mech.* **39**, 101–110.

SOMMERIA, J., MEYERS, S. D. & SWINNEY, H. L. 1991 Experiments on vortices and Rossby waves in eastward and westward jets. In *Nonlinear Topics in Ocean Physics* (ed. A. R. Osborne), Enrico Fermi International School of Physics, vol. 109, pp. 227–269. North-Holland.

SURI, B., TITHOF, J., GRIGORIEV, R. O. & SCHATZ, M. F. 2017 Forecasting fluid flows using the geometry of turbulence. *Phys. Rev. Lett.* **118**, 114501.

TAGG, R. 1994 The Couette–Taylor problem. *Nonlinear Sci. Today* **4**, 1–25.

TAVENER, S. J., MULLIN, T. & CLIFFE, K. A. 1991 Novel bifurcation phenomena in rotating annulus. *J. Fluid Mech.* **229**, 483–497.

TAYLOR, G. I. 1936*a* Fluid friction between rotating cylinders. I. Torque measurements. *Proc. R. Soc. Lond.* A **157**, 546–564.

TAYLOR, G. I. 1936*b* Fluid friction between rotating cylinders. II. Distribution of velocity between concentric cylinders when outer one is rotating and inner one is at rest. *Proc. R. Soc. Lond.* A **157**, 565–578.

VAN ATTA, C. 1966 Exploratory measurements in spiral turbulence. *J. Fluid Mech.* **25**, 495–512.

WENDT, F. 1933 Turbulente Strömungen zwischen zwei rotierenden konaxialen Zylindern. *Ing.-Arch.* **4**, 577–595.